Spectromicroscopic measurement of surface and bulk band structure interplay in a disordered topological insulator

Erica Kotta,[1] Lin Miao,[1,2] Yishuai Xu,[1] S. Alexander Breitweiser,[1,3] Chris Jozwiak,[2] Aaron Bostwick,[2] Eli Rotenberg,[2] Wenhan Zhang,[4] Weida Wu,[4] Takehito Suzuki,[5] Joseph Checkelsky,[5] and L. Andrew Wray,[1]*

[1] Department of Physics, New York University, New York, New York 10003, USA
[2] Advanced Light Source, Lawrence Berkeley National Laboratory, Berkeley, CA 94720, USA
[3] Department of Physics and Astronomy, University of Pennsylvania, Philadelphia, PA 19104, USA
[4] Rutgers Department of Physics and Astronomy, Rutgers University, Piscataway New Jersey 08854, USA
[5] Massachusetts Institute of Technology, Department of Physics, Cambridge, MA, 02139, USA

* To whom correspondence should be addressed; E-mail: lawray@nyu.edu.

Topological insulators are bulk semiconductors that manifest in-gap surface states with massless Dirac-like dispersion due to the topological bulk-boundary correspondence principle [1-3]. These surface states can be manipulated by the interface environment to display various emergent phenomena [4-11]. Here, we use angle-resolved photoemission spectroscopy (ARPES) and scanning tunneling microscopy (STM) to investigate the interplay of crystallographic inhomogeneity with the topologically ordered band structure in a model topological insulator. We develop quantitative analysis methods to obtain spectroscopic information in spite of a limited dwell time on each measured point. We find that the band energies vary on the scale of 50 meV across the sample surface, and this enables single-sample measurements that are analogous to a multi-sample doping series. By focusing separately on the bulk and surface electrons we reveal a hybridization-like interplay between fluctuations in the surface and bulk state energetics.

The three-dimensional topological insulator (TI) state in Bi_2Se_3 was identified in 2008 [12,13] and features a large bulk band gap of ~0.3eV, spanned by a relatively ideal Dirac cone surface state. Though the existence of the surface state is protected by topology, the symmetries and band dispersion of surface state electrons can be strongly influenced by crystallographic defects, potentially including the emergence of new quasiparticles [7-11,14-18, 22]. Bulk grown samples also feature inhomogeneity on the 1-1000 μm scale, and the diversity of chemical potential, lattice strain, and disorder at this scale encodes tremendous information about the electronic system that would be difficult to reproduce through the deliberate control of doping, strain, or other experimental parameters [23]. A major purpose of this investigation is to explore rigorous procedures for utilizing intrinsic inhomogeneity to understand the variability of Dirac electronic structures (see summary of analysis procedures in Methods).

The central region of the sample surface, exposed by *in situ* cleavage, was mapped in 961 individual ARPES images covering a 31 x 31 grid with uniform 10 μm spacing. A dwell time of just 2s/point was used to avoid surface aging (band bending [19]) from the highly focused incident photon beam (see characterization in Supplementary Fig. S1). Binning all 961 measurements results in a high-statistics Dirac cone image that is equivalent to a conventional ARPES measurement performed with a .3 x .3 mm^2 beam spot (Fig. 1a). An example of a single-

point 2s spectrum is shown in Fig. 1b, with the otherwise sparse data broadened for visibility. A V-shaped upper Dirac cone can be immediately identified in most single-point ARPES spectra, but the statistics are inadequate for a close analysis without first leveraging information from the rest of the surface.

To map out the variation in the surface state electronic structure across the sample surface, a small window around the Dirac point of the spatially averaged ARPES image (red box in Figure 1a) is used as a template for normalized cross-correlation with each single-scan spectrum (see Supplementary Note 3). The Dirac point coordinate $\{E_D,k_D\}$ is identified from a sharp peak in the cross-correlation map (Fig. 1c), yielding surface maps shown in Fig. 2a,c. As the Dirac point is constrained by symmetry to always be located in the Brillouin zone center, shifts in k_D actually represent changes in the orientation of the surface, which changes the angle of surface-normal (k=0) photoemission.

Shifting each ARPES image along the momentum axis ($k_{||}$-axis) to set k_D=0 therefore allows for a more meaningful binning of the images and makes it feasible to fit other quantities such as the *bulk* band energies. For example, by examining a constant-momentum energy dispersion curve (EDC) evaluated at k_D, one can fit the onset of intensity with a step function to determine the bulk conduction band minimum energy (map in Fig. 2b). Beyond these maps of binding energy, evaluating scattering intensity in a small {E,k} range centered around the cross-correlation maximum $\{E_D,k_D\}$ point offers a quick diagnostic tool to identify anomalous regions in which the surface state less closely resembles an ideal Dirac cone (Fig. 2d).

The resulting maps of these four properties reveal very different forms of spatial structure on the sample surface. The map of Dirac point momentum (k_D, Fig. 2c) shows a gently warped surface with continuous gradations and few sharp boundaries. Two triangular regions, shaded in gray, show a much rougher topography and are chosen by hand to be excluded from further analysis (see Supplementary Fig. 3). The Dirac point energy map (Fig. 2a) shows a significant ~50 meV distribution, with 50% of the surface lying within 10 meV of the average E_D~430 meV binding energy. Larger binding energies are found in several ~50 μm diameter islands, and a strip with smaller binding energy runs ~20-120 μm above the bottom edge of the sample.

The bulk band energy map (Fig. 2b) reveals fluctuations on approximately the same ~50 meV scale as the surface Dirac point, and a similar horizontal trough feature with small binding energies is also recognizable ~20-120 μm above the bottom edge. Other than this, surface regions look qualitatively different from the Dirac point energy map, and regions with larger bulk binding energy show limited correlation between the two maps, as we will see in Figures 3-4. The Dirac point intensity map (Fig. 2d) is smoothest of all, showing a flat surface transected by three dark stripe-like features running diagonally downwards from left to right. These are most likely caused by buckling of the sample along the y-axis, which causes the measurement to slightly miss the Dirac point in 2D momentum space (see Supplementary Fig. 3b). Faint shadows of these 3 features are also observable in the Dirac point momentum (k_D) map in Fig. 2c; however, only the feature in the lower left corresponds with a clear feature in the bulk and surface energy maps in Fig. 2a-b.

Supplementary STM measurements were performed to investigate the chemical origin of these variations in binding energy and confirm that point defect populations vary greatly across the surface. Four ≥ 100 x 100 nm^2 surface regions separated by ~0.5 mm were measured on a sample from the same growth batch (see Supplementary Figure 5), revealing that charge-donating point defects within 1 nm of the surface are primarily intercalated excess Se (Se_i) and Se replacement sites (Bi_{Se}) associated with excess Bi. The densities of these two defect types were strongly anticorrelated, representing inhomogeneity in the relative local density of Bi and Se (see Supplementary Table 1). On average, there was a stoichiometric excess of 0.0014 Bi atoms per 5-atom unit cell, with a standard deviation of 0.0004 (±30%) for different sampled regions, sufficient to greatly influence the chemical potential and surface state energetics [7,8] (see also Supplementary Note 5 discussion).

Having corrected for the surface curvature, the large fluctuations we observe in bulk and surface binding energies can now be used to organize the data in a way that resembles a doping series, but which we will term a “binning series.” Figure 3a-d shows composite spectra obtained from binning measurements with similar Dirac point binding energy. Spectra are labeled with the average Dirac point energy of the measurements binned within them, and the k=0 EDC of each spectrum is shown to the right (Fig. 3e). A similar series binning from the bulk energy map

is displayed below in Fig. 3f-i. The single-point measurements used for the two binning series are indicated via a color code in histograms (Fig. 3j,k) and on the marked surface maps (Fig. 3l,m).

The Dirac point series EDCs (Fig. 3e) show a peak at the Dirac point energy that nicely tracks the average bin energy. However, the onset of the bulk conduction band at E_B~0.23 eV binding energy shows surprisingly little dependence on the Dirac point energy, suggesting that different factors may be responsible for the fluctuations in bulk and surface bands. Larger bin widths were used in the bulk binning series (see Fig. 3k histogram), for which we will briefly discuss bias effects intrinsic to this presentation of the data. Each image in the bulk series (Fig. 3f-h) is labeled with the energy center of mass, and these numbers span a 32 meV range. However, these numbers are biased, due to the points being drawn with some error from a peaked distribution. A conservative estimate of this bias can be obtained by characterizing the error in the fitting procedure, then evaluating the convolution of this error with the distribution from which the measurement is sampled (see Supplementary Note 4). This results in bias-corrected bin energies with just a 20 meV distribution (0.227, 0.240, and 0.247 eV for Fig. 3f-h, respectively). Less error is expected in the Dirac point series, due to the smaller bin sizes and slightly superior fitting error.

To better understand the interplay between bulk and surface energetics, it is useful to resolve how surface state energies in different parts of momentum space change in response to this 20 meV shift of the bulk band. The change in intensity at the leading edge of the surface state can be used to estimate this shift, as $\Delta E_S(k)=[I(E,k)_h - I(E,k)_f] \div [\partial I(E,k)_{avg}/\partial E]$. Here, $I(E,k)_{f,h}$ indicates the ARPES data in Fig. 3f and 3h, respectively, and 'avg' indicates an average over the spectra in panels 3f-h. The results are summarized in Fig. 4a, where the length of the blue arrows is set proportional to the magnitude of the surface state energy shift at that momentum. An alternative analysis method is presented in the Supplementary Fig. 6 and shows roughly equivalent results.

The picture obtained is intriguingly non-uniform. Surface energy shifts are relatively large (>10 meV from Fig. 4a) for $|k| > 0.007$ Å^{-1} and $|k| < 0.003$ Å^{-1}, corresponding to a ~55% correlation with the 20-meV bulk band shift. At the intermediate values 0.003 Å^{-1} $< |k| < 0.007$

$Å^{-1}$ where the surface state falls in the middle of the bulk band gap, the shifts dip beneath 7 meV (Fig. 4a), indicating a smaller ~35% correlation. The observation that the surface state moves in tandem with the bulk band near the Fermi level and Dirac point while being less correlated at the intermediate momenta can be partially understood from the fact that the surface state is intrinsically hybridized with the bulk continuum, inducing a greater correlation with the bulk energetics. Near the Fermi level, the surface state runs along the external contour of the bulk conduction band with a near-parallel trajectory [6] and shifts strongly and uniformly in tandem with the changing bulk binding energy. At larger binding energies near the Dirac point, strong hybridization is again expected, now from proximity to the bulk *valence* band. In Fig. 4b, a tight-binding model for Bi_2Se_3 (see Supplementary Note 7) is used to investigate the numerical derivative of surface state energy as the bulk energy is shifted ($dE_S(k)/dE_B$), with mid-gap surface state energy held fixed to enhance contrast. Bulk energy was controlled by increasing the binding energy of all orbitals beneath the outermost quintuple layer, resulting in a downward distortion of portions of the surface state that were energetically close to the bulk bands. A maximum amplitude of $dE_S(k)/dE_B$ = 18% is seen at the Fermi level, corresponding to the expected difference between the surface-bulk energy correlation at the Fermi level and middle of the bulk band gap. This value is remarkably close to the ~20% difference seen within the experimental data, suggesting that a hybridization-based interpretation can plausibly account for the evolution of the surface state across the bulk binning series.

A further prediction one can draw within this picture is that when the bulk bands have large binding energy and are thus 'pulled away' from the surface Dirac point, bulk-surface energy correlations at the Dirac point should become smaller. Figure 4c shows a histogram of the surface Dirac point (E_S) versus bulk (E_B) energies, with the center of mass trend traced as a function of bulk energy (dashed purple line). Center of mass coordinates are plotted for each bulk energy bin with more than 10 measurements, using a larger step near the edges to maintain a minimum number of measurements per point. This trend curve has a significant slope at the center of the bulk binning series (E_B=0.24 eV), which increases as the bulk band is brought to smaller binding energy (to E_B~0.19 eV), and flattens out as it is brought to larger binding energies, matching expectations for a hybridized picture (solid blue line). A kink in the

trend curve at E_B~0.18 eV is also present in the simulation, where it occurs due to the transition of the Dirac point from a true in-gap surface state to a bulk-degenerate 'resonance state'.

The observation of this hybridization-like interplay between the bulk and surface states provides a significant ingredient for understanding the electron system at a topological insulator surface, and for predicting dynamical phenomena such as surface-bulk electronic scattering that has been noted in recent pump-probe ARPES investigations [24-25]. The presentation of hybridization as an experimental observable stems from a new paradigm that emerges when applying the ARPES technique as spectromicroscopy. Rather than a single clear image, the spectromicroscopy data set is composed of a large continuum-like set of spatially resolved images, each containing relatively sparse data. By organizing these data into a "binning series", we recover a close analogue to a conventional doping series, but with a few key differences. As a disadvantage, new procedures must be implemented to understand error and the sensitivity of the binned images to sampling bias. However, as an advantage, the variability of the material is resolved from looking at a single sample, and on a perturbative ~10 meV energy scale that would be difficult or impossible to achieve across multiple sample batches through deliberate control of growth conditions. Moreover, there are multiple parameters that one can draw on to create doping series representations of the same data set. This enables the observation of conditional relationships between different distinct features of the electronic structure, such as occur through hybridization and strong many-body interactions.

Methods

Sample growth, characterization and measurement

The sample was grown following standard procedures of [20,21], but with an abbreviated annealing process of 24 hours (compared to the standard ~3 days) to achieve a single-phase sample that retains a relatively high defect density. The sample was cleaved and measured *in situ* at low temperature (T~20K) and ultra-high vacuum (<5×10^{11} Torr) at the microARPES endstation of the Advanced Light Source MAESTRO 7.0.2 Beamline. Measurements were performed with a photon energy of 110 eV, and photoelectrons were passed through a Scienta

R4000 electron analyzer for an energy and momentum resolution better than 30 meV and 0.01 $Å^{-1}$, respectively. The illuminated beam spot was smaller than δ~<15 μm in diameter. All measurements were performed along the Γ-K momentum axis of the hexagonal surface Brillouin zone, along which the Dirac cone appears as a V-shaped contour centered at the Γ point. The measurements made use of π-polarization (predominantly out-of-plane), which maximizes the overall ARPES signal, but has been suggested to give greater spectroscopic weight to surface regions with a lower defect density [8].

Summary of analysis procedures

The analysis procedures demonstrated here can be adopted independently, but also constitute a sequentially cumulative recipe, using the following procedural order:

1. **Normalization:** Represent ARPES intensity in terms of the number of recorded photoelectrons I(E,k) (see Supplementary Note 2). A simple pixel-intensity unit calibration mask can suffice. This step is the prerequisite for simulating analysis/fitting approaches to achieve quantitative error bars (see Supplementary Note 3).

2. **Cross-correlation:** Track the energy and momentum coordinates of the Dirac point by calculating the normalized cross-correlation (X(E,k), see Supplemental Note 3) of a manually selected region of interest from the spatially-averaged, high-statistics spectral data (the "template") to each individual ARPES image, associating the maximum correlation value's (E,k) coordinates with the Dirac point. Error bars can be obtained by simulating the cross-correlation procedure, or from the standard deviation of regional fluctuations (see Supplementary Figure 4a). This step is also the prerequisite for applying momentum-axis corrections.

3. **Fit/Extract other band properties:** Correct all data with the momentum shifts obtained in step 2, and then apply additional measurements/fits to this data set. Examples in the paper include Dirac point intensity mapping, and bulk band energy fitting. A quantitative error estimate can be obtained from simulating the measurement based on a normalized template (see Supplementary Figure 4b,c).

4. **Create composite spectra:** Histogram the measurements as a function of individual quantities extracted in steps 2-3 (e.g. Dirac point energy), and create composite spectra to evaluate how band structure varies as a function of that quantity. If the histogram distribution is sharply peaked (not flat across composite bins), then it is vital to correct for sampling error as discussed in Supplementary Note 4.

End Notes

Acknowledgements:

This research used resources of the Advanced Light Source, which is a DOE Office of Science User Facility under contract no. DE-AC02-05CH11231. Work at NYU was supported by the MRSEC Program of the National Science Foundation under Award Number DMR-1420073. Synthesis and analysis instrumentation at NYU is supported by NSF under MRI-1531664, and by the Gordon and Betty Moore Foundation's EPiQS Initiative through Grant GBMF4838. The STM work at Rutgers is supported by NSF under grant DMR-1506618. This research is funded in part by the Gordon and Betty Moore Foundation EPiQS Initiative, Grant GBMF3848 to JGC (instrumentation development) and Office of Naval Research (ONR) under Award N00014-17-1-2883 (material synthesis).

Author Contributions:

E.K., L.M., Y.X., and S.A.B. carried out the ARPES experiments, with support from C.J., A.B., and E.B.; STM experiments were performed by W.Z., with guidance from W.W.; high quality samples were synthesized by T.S, with guidance from J.C.; computational data analysis and tight binding simulations were implemented by E.K. and Y.X., with assistance from S.A.B., and L.A.W.; E.K., L.M., Y.X., and L.A.W. participated in the analysis, figure planning and draft preparation; L.A.W. was responsible for the conception and the overall direction, planning and integration among different research units.

Competing interests:

The authors declare no competing financial or non-financial interests.

Data availability:

The data represented in Figs. 1c, 2, 3e, 3i-m, and 4c are available as source data with the online version of the paper. All other data that support the plots within this paper and other findings of this study are available from the corresponding author upon reasonable request.

Code availability:

All relevant source code or algorithms are available from the corresponding authors upon reasonable request.

References

[1] Hasan, M. Z. & Kane, C. L. Colloquium: Topological insulators. *Rev. Mod. Phys.* **82**, 3045-3049 (2010).

[2] Qi, X.-L. & Zhang, S.-C. Topological insulators and superconductors. *Rev. Mod. Phys*. **83**, 1057-1067 (2011).

[3] Fu, L., Kane, C. L. & Mele, E. J. Topological insulators in three dimensions. *Phys. Rev. Lett*. **98**, 106803 (2007).

[4] Qi, X.-L. et al. Inducing a magnetic monopole with topological surface states. *Science* **323**, 1184–1187 (2009).

[5] Fu, L. & Kane, C. L. Superconducting proximity effect and Majorana fermions at the surface of a topological insulator. *Phys. Rev. Lett*. **100**, 096407 (2008).

[6] Wray, L. A. et al. Observation of topological order in a superconducting doped topological insulator. *Nat. Phys.* **6**, 855-859 (2010).

[7] Xu, Y. et al. Disorder enabled band structure engineering of a topological insulator surface. *Nat. Comm.* **8**, 14081 (2017).

[8] Miao, L. et al. Observation of a topological insulator Dirac cone reshaped by non-magnetic impurity resonance. *NPJ Quantum Materials* **3**, 29 (2018).

[9] Alpichshev, Z. et al. STM imaging of impurity resonances on Bi_2Se_3. *Phys. Rev. Lett.* **108**, 206402 (2012).

[10] Alpichshev, Z. et al. STM imaging of electronic waves on the surface of Bi_2Te_3: topologically protected surface states and hexagonal warping effects. *Phys. Rev. Lett.* **104**, 016401 (2010).

[11] Xu, Y. et al. Connection topology of step edge state bands at the surface of a three dimensional topological insulator. *New J. Phys.* **20**, 073014 (2018).

[12] Zhang, H. et al. Topological insulators in Bi_2Se_3, Bi_2Te_3 and Sb_2Te_3 with a single Dirac cone on the surface. *Nat. Phys.* **5**, 438-442 (2009).

[13] Xia, Y. et al. Observation of a large-gap topological-insulator class with a single Dirac cone on the surface. *Nat. Phys*. **5**, 398-402 (2009).

[14] Biswas, R. R. & Balatsky, A. V. Impurity-induced states on the surface of three-dimensional topological insulators. *Phys. Rev. B* **81**, 233405 (2010).

[15] Beidenkopf, H. et al. Spatial fluctuations of helical Dirac fermions on the surface of topological insulators. *Nat. Phys*. **7**, 939–943 (2011).

[16] Black-Schaffer, A. M. & Balatsky, A. V. Subsurface impurities and vacancies in a three-dimensional topological insulator. *Phys. Rev. B* **86**, 115433 (2012).

[17] Black-Schaffer, A. M. & Yudin, D. Spontaneous gap generation on the surface of weakly interacting topological insulators using nonmagnetic impurities. *Phys. Rev. B* **90**, 161413(R) (2014).

[18] Zhong, M. et al. Effect of impurity resonant states on optical and thermoelectric properties on the surface of a topological insulator. *Sci. Rep*. **7**, 3971 (2017).

[19] Frantzeskakis, E. et al. Trigger of the ubiquitous surface band bending in 3d topological insulators. *Phys. Rev. X* **7**, 041041 (2017).

[20] Hyde, G. R., Beale, H. A., Spain, I. L. & Woollam, J. A. Electronic properties of Bi_2Se_3 crystals. *J. Phys. Chem. Solids* **35**, 1719-1728 (1974).

[21] Hor, Y. et al. Superconductivity and non-metallicity induced by doping the topological insulators Bi_2Se_3 and Bi_2Te_3. *J. Phys. Chem. Solids* **72**, 572-576 (2011).
[22] Kastl, C. et al. Effects of defects on band structure and excitons in WS_2 revealed by nanoscale photoemission spectroscopy. *ACS Nano* **13**, 1284-1291 (2019).
[23] Schwier, H. et al. Applications for ultimate spatial resolution in LASER based u-ARPES: A FeSe case study. AIP Conference Proceedings **2054**, 040017 (2019);
[24] Hajlaoui, M. et al. Ultrafast surface carrier dynamics in the topological insulator Bi_2Te_3. *Nano Lett.* **12**, 3532-3536 (2012).
[25] Sobota, J. A. et al. Ultrafast optical excitation of a persistent surface-state population in the topological insulator Bi_2Se_3. *Phys. Rev. Lett.* **108**, 117403 (2012).

Figure 1: Cross-correlation for ARPES analysis. a, A composite spectrum obtained by summing all data from a 31x31 point spectromicroscopy map of the sample surface. A red square enclosing the surface state Dirac point indicates the data window used as a template for cross correlation. **b,** An individual scan is overlaid with the template cut-out from panel (a). Gaussian broadening with a half-width of 13 meV and 0.015 $Å^{-1}$ is applied for visibility. **c**, The energy- and momentum-space location of the surface Dirac point can be seen from a sharp peak in the normalized cross-correlation of the composite template with the individual scan data from panel (b).

Figure 2: Real space maps of electronic band structure. a, The surface state Dirac point binding energy. **b,** The bulk conduction band (BCB) energy minimum, with data smoothed by adding 25% of the nearest neighbor pixel intensities. Error bars for panels (a-b) are <~10 meV (see Supplementary Note 4). **c**, The relative shift of the Dirac point on the $k_{||}$-axis of momentum space, representing the direction of the surface-normal cleavage axis. **d**, Spectral intensity at the Dirac point. The gray shaded regions do not contain a Dirac-cone-like spectral feature and are excluded from detailed analysis.

Figure 3: Bulk- and surface-ordered binning series. a-d, Composite ARPES spectra created by binning measurements with Dirac point energies in successive 10 meV regions. The average Dirac point energy is labeled for each image. **e,** Constant momentum profiles of spectral intensity (EDCs) in the Brillouin zone center taken from the spectra a-d. Grey arrows indicate the bulk band onset energy, and magenta arrows indicate the Dirac point energy. Templates used for fitting are shown as black dashed lines. **f-h,** ARPES spectra with bulk binding energies within wider, variable-width ranges are binned together and labeled with the average bulk band energies of the corresponding bin. **i,** Brillouin zone center EDCs for f-h. **j-k,** Histograms of the observed (j) Dirac point and (k) bulk energies are color-coded to indicate the regions used for binning series panels. **l-m**, Maps of surface and bulk energies are color-coded as defined on the panel (j-k) histograms to indicate their incorporation within the binning series sets.

Figure 4: Interplay of bulk and surface electronic states. a, A summary image showing how different portions of the surface state shift in energy across the bulk band binning series. The length and thickness of the arrows are scaled linearly with the magnitude of the energy shift of the surface band at that momentum across the bulk binning series, with an amplitude of ΔE_S=11 meV attributed at the Fermi level ($\Delta E_S/\Delta E_B$ ~ 55% = 11/20). **b,** A simulation of the repulsion between surface and bulk bands, with the mid-gap surface state (at k = 0.05$Å^{-1}$) set to a fixed binding energy. Arrows show the fractional energy shift in response to the change in bulk energies (dE_S/dE_B = 18% at the Fermi level) when a uniform potential is applied to all orbitals beneath the outermost quintuple layer. **c,** A 2D histogram of the observed Dirac point and bulk conduction band energies is overlaid with a purple trend curve showing the E_B-resolved center of mass (see text). Error bars represent propagated single-point measurement error. A simulation of Dirac point (DP) energy versus bulk energy is plotted in blue. At E_B<~0.18 eV the modeled spectral feature leaves the band gap and becomes a bulk-degenerate resonance state (DP res).

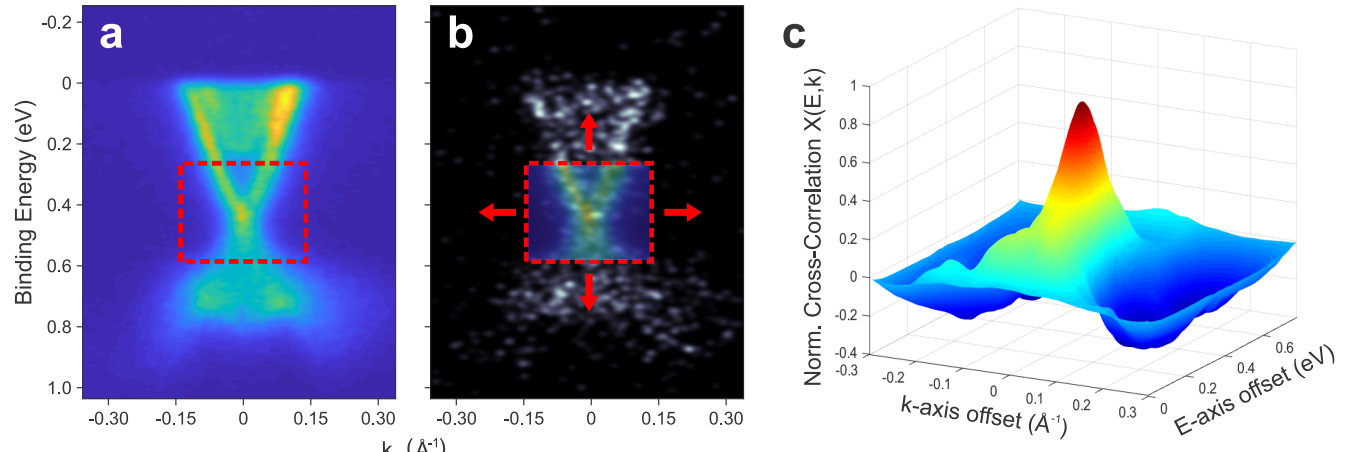
a
b
c
Binding Energy (eV)
-0.2
0
0.2
0.4
0.6
0.8
1.0
-0.30
-0.15
0
0.15
0.30
k∥ (Å-1)
Norm. Cross-Correlation X(E,k)
1
0.8
0.6
0.4
0.2
0
-0.2
-0.4
-0.3
-0.2
-0.1
0
0.1
0.2
0.3
k-axis offset (Å-1)
0
0.2
0.4
0.6
E-axis offset (eV)

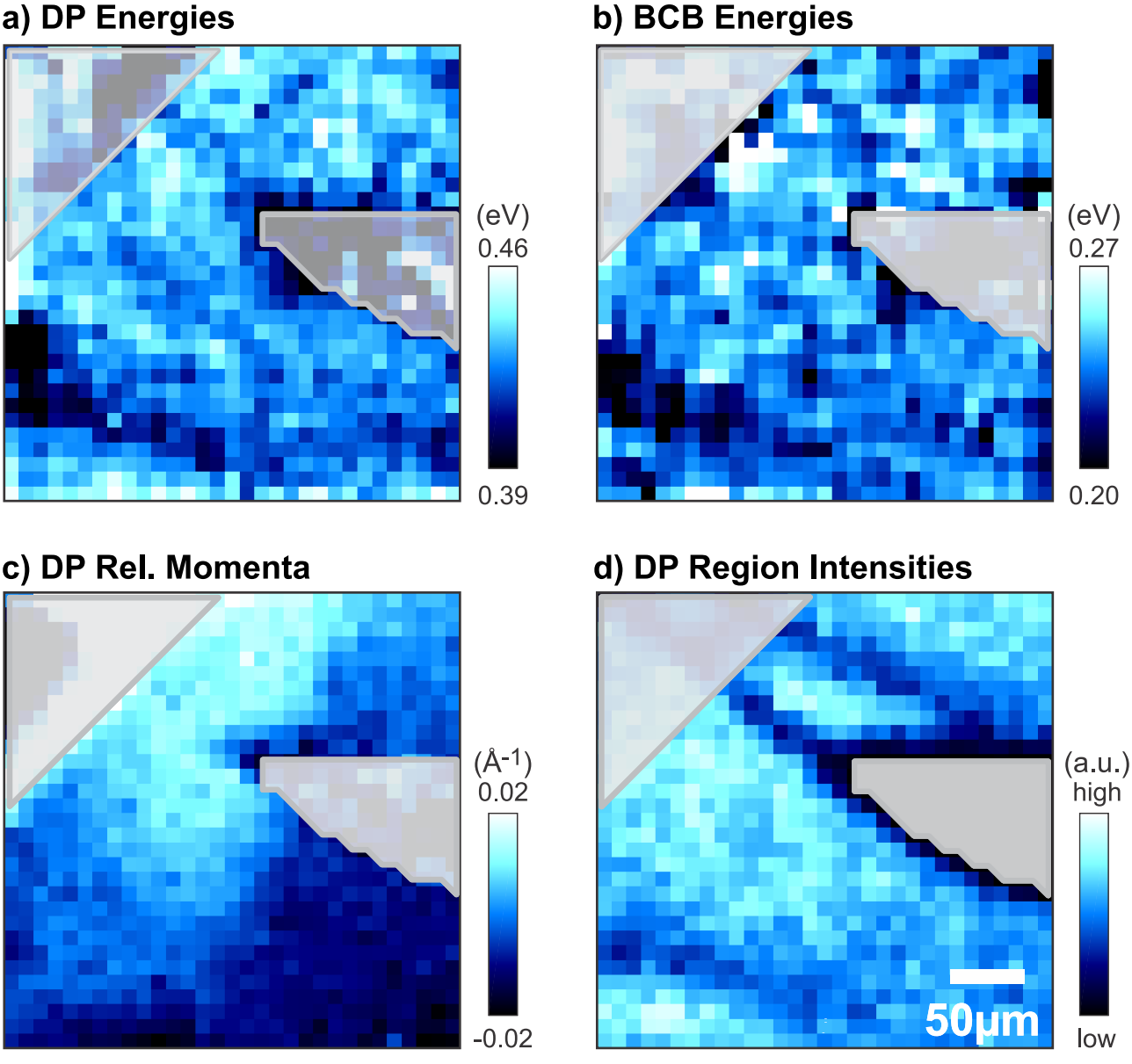
a) DP Energies
(eV)
0.46
0.39
b) BCB Energies
(eV)
0.27
0.20
c) DP Rel. Momenta
(Å-1)
0.02
-0.02
d) DP Region Intensities
(a.u.)
high
low
50µm

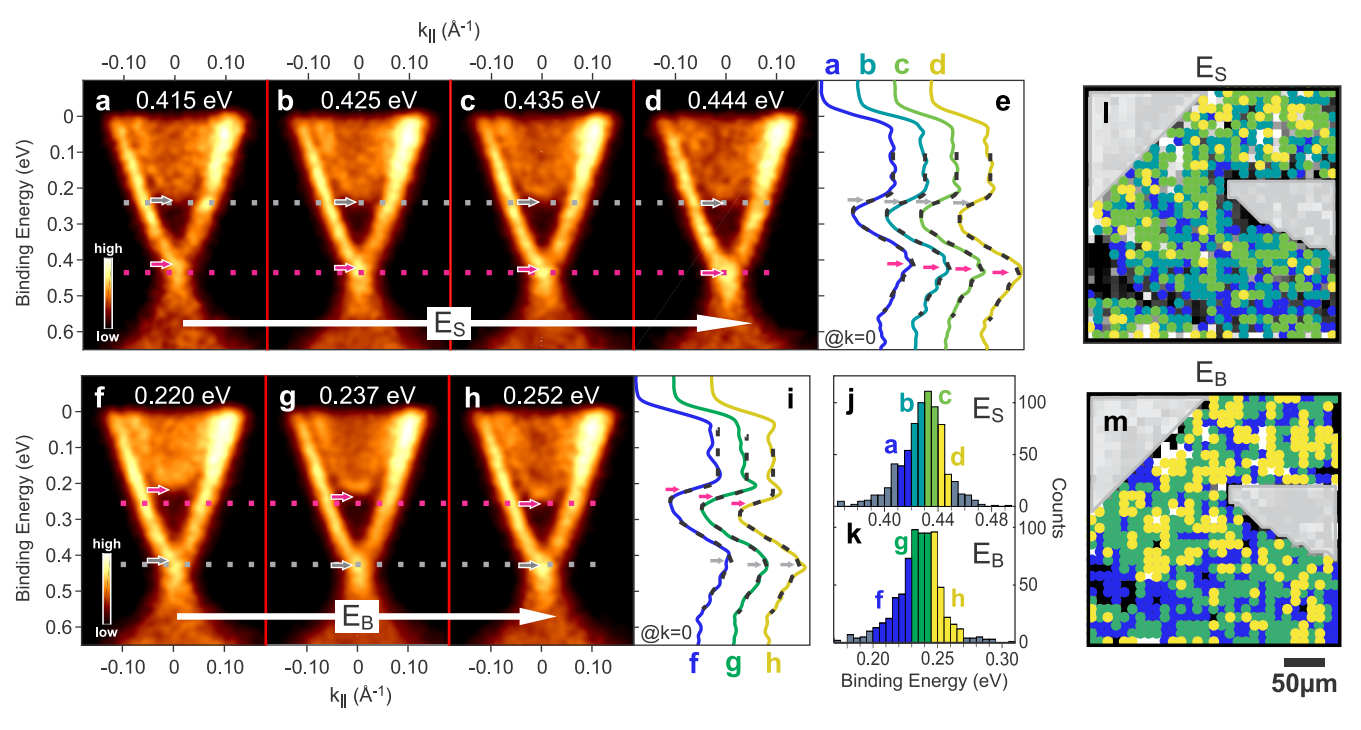
k∥ (Å-1)
-0.10 0 0.10
a 0.415 eV
b 0.425 eV
c 0.435 eV
d 0.444 eV
e
@k=0
Binding Energy (eV)
high
low
ES
f 0.220 eV
g 0.237 eV
h 0.252 eV
i
EB
j
k
Counts
Binding Energy (eV)
l
m
50μm

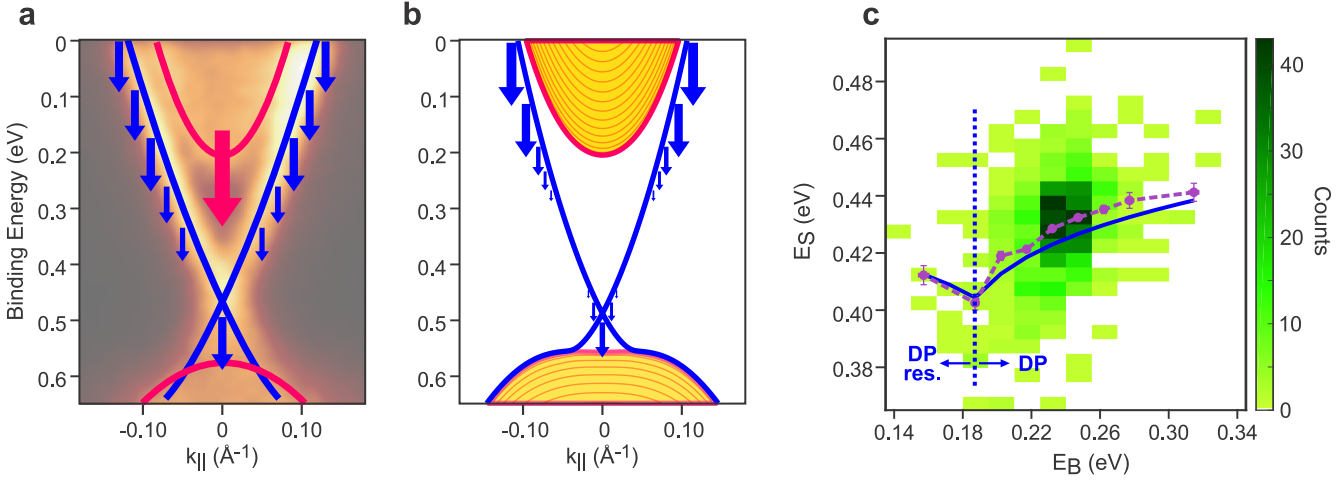
a
b
c
Binding Energy (eV)
0
0.1
0.2
0.3
0.4
0.5
0.6
-0.10
0
0.10
k|| (Å-1)
ES (eV)
0.48
0.46
0.44
0.42
0.40
0.38
0.14
0.18
0.22
0.26
0.30
0.34
EB (eV)
DP
res.
DP
Counts
40
30
20
10
0